

Toward Automatic Subsurface Pipeline Mapping by Fusing a Ground-Penetrating Radar and a Camera

Haifeng Li¹, Chieh Chou², *Student Member, IEEE*, Longfei Fan, Binbin Li,
Di Wang, and Dezhen Song³, *Senior Member, IEEE*

Abstract—We propose a novel subsurface pipeline mapping and 3D reconstruction method by fusing ground-penetrating radar (GPR) scans and camera images. To facilitate the simultaneous detection of multiple pipelines, we model the GPR sensing process and prove hyperbola response for general scanning with nonperpendicular angles. Furthermore, we fuse visual simultaneous localization and mapping outputs, encoder readings with GPR scans to classify hyperbolas into different pipeline groups. We extensively apply the J-linkage method and maximum likelihood estimation with error analysis to improve algorithm robustness and accuracy. As a result, we optimally estimate the radii and locations of all pipelines. We have implemented our method and tested it in physical experiments with representative pipeline configurations. Two different kinds of 3-m-long pipes are used, with radii being 4.62 and 3.02 cm, respectively. The results show that our method successfully reconstructs all subsurface pipes. Moreover, the average estimation errors for two orientation angles of pipelines are 1.73° and 0.73° , respectively. The average localization error is 4.47 cm.

Note to Practitioners—Automatic and accurate underground pipeline mapping technology is very important in civil construction projects. Lack of 3D utility pipeline maps may lead to accidental damage in civil construction and maintenance. Although ground-penetrating radar (GPR)-based pipeline mapping methods have been studied for several years, these methods require the perpendicular scanning with respect to the pipe, which is impossible to guarantee in practice since the orientations of pipelines are unknown. Furthermore, these traditional methods can only estimate one pipeline at a time in a survey area and require prior knowledge of pipe diameter. We propose a robotic subsurface pipeline mapping method with a GPR and a camera to

handle difficult factors such as multiple pipes, unknown pipeline orientation, and unknown pipeline diameters. Hence, we can perform GPR scanning along any generic linear trajectories. Our method has been tested in physical experiments with representative pipeline configurations. The results are sufficiently accurate, and it proves that our method can be an effective technology to reconstruct the underground pipelines.

Index Terms—Ground-penetrating radar (GPR) and camera sensor fusion, hyperbola detection, underground pipeline mapping.

I. INTRODUCTION

PRECISE 3D maps for underground pipelines, such as gas, water, and sewage pipes, are important for local governments, utility companies, and civil engineers. However, underground pipeline locations in old urban areas are usually unknown. Even in new urban areas, there are no 3D maps but rough 2D layout information [1] for subsurface pipelines. As a result, civil construction projects can easily damage underground pipes and cause significant loss. A ground-penetrating radar (GPR) is an important tool for the detection and localization of underground objects. However, a GPR does not directly provide a 3D position but convoluted and noisy radar reflection images which require trained eyes to manually recognize objects of interest. For pipeline mapping, the traditional GPR methods [2]–[5] have too many limitations and constraints; only allow one pipeline in a survey area, require prior knowledge of pipe diameter or orientation, and only perform perpendicular scanning with respect to the pipe. Therefore, the whole process is labor intensive and costly.

To automate the pipeline mapping problem, we propose a new method to simultaneously map multiple subsurface pipelines using a GPR and a camera (see Fig. 1). We model the GPR sensing process and prove/derive hyperbola responses for general scanning with nonperpendicular angles. This allows us to develop a new hyperbola detection algorithm for multiple pipeline detection. Next, we fuse visual simultaneous localization and mapping (vSLAM) outputs and encoder readings with GPR scans to classify hyperbolas into groups belonged to different pipelines. We extensively apply the J-linkage method [6] and the maximum likelihood estimation (MLE) to improve the algorithm robustness and accuracy. As a result, we optimally estimate the radii and locations of all pipelines. We have implemented our method and tested it in physical experiments. Two different kinds of 3-m-long pipes

Manuscript received May 6, 2019; revised August 5, 2019; accepted September 5, 2019. This article was recommended for publication by Associate Editor Q. Xu and Editor Y. Sun upon evaluation of the reviewers' comments. This work was supported in part by the National Science Foundation under Grant NRI-1526200, Grant 1748161, and Grant 1925037, in part by the National Science Foundation of China under Grant 61305107, in part by Industrial Robot Application of Fujian University Engineering Research Center, Minjiang University, under Grant MJUKF-IRA201803 and Grant MJUKF-IRA201807, and in part by the Chinese Scholarship Council. (*Corresponding author: Dezhen Song.*)

H. Li and L. Fan are with the Department of Computer Science, Civil Aviation University of China, Tianjin 300300, China, and also with the Industrial Robot Application, Fujian University Engineering Research Center, Minjiang University, Fuzhou 350108, China (e-mail: hfli@cauc.edu.cn).

C. Chou, B. Li, D. Wang, and D. Song are with the Department of Computer Science and Engineering, Texas A&M University, College Station, TX 77843 USA (e-mail: cchou@tamu.edu; binbinli@tamu.edu; ivanwang@tamu.edu; dzsong@cse.tamu.edu).

This article has supplementary downloadable material available at <http://ieeexplore.ieee.org>, provided by the authors.

Color versions of one or more of the figures in this article are available online at <http://ieeexplore.ieee.org>.

Digital Object Identifier 10.1109/TASE.2019.2941848

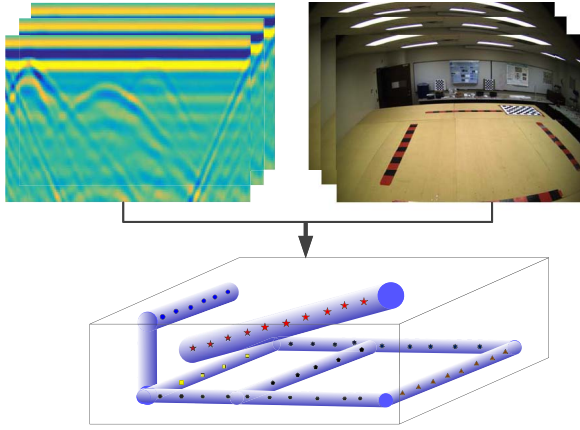


Fig. 1. Illustration of our subsurface pipeline mapping problem. Given a set of GPR scans and camera images, our algorithm outputs a set of collinear center axis points and radii of all buried pipelines. The reconstructed 3D points are represented with different marks according to their residing pipelines.

are used, with radii being 4.62 and 3.02 cm, respectively. The results show that our method successfully reconstructs all subsurface pipes. Moreover, the average estimation errors for two orientation angles of pipelines are 1.73° and 0.73° , respectively. The average localization error is 4.47 cm.

The rest of the article is organized as follows. We summarize the related work in Section II before we introduce our pipeline mapping problem in Section III. We detail our algorithm design in Section IV. We perform the algorithm computational complexity analysis in Section V. We test our algorithm in experiments in Section VI and conclude our article in Section VII.

II. RELATED WORK

Pipeline mapping is a critical step for assessing the condition of the buried utility pipelines. There are many existing efforts focusing on condition assessment [7] in general. The 3D reconstruction for the cylinder pipeline above the ground has been well studied [8], where laser scanner can be used to generate a point cloud of pipeline surface. However, laser scanner cannot be adopted to detect underground pipelines. Popular approaches for buried pipeline mapping include electromagnetic, acoustic, and seismic methods. A U.K. project named Mapping the Underworld [9] focuses on locating, mapping, and recording buried utility assets by fusing multiple sensors.

Among different sensor modalities, GPRs have been widely used in subsurface target detection [10]–[12]. However, mapping the underground targets from GPR signals is nontrivial, because different from a laser scanner, a GPR cannot provide 3D positions but a reflection image with high degrees of freedom (DoFs) for interpretation. Windsor *et al.* [2] estimate subsurface pipe diameters with a given radio propagation velocity. Al-Nuaimy *et al.* [3] estimate pipeline depth by assuming zero pipeline radius and a perpendicular scanning trajectory. The assumptions limit their methods to cases when the pipeline is buried very deep and with small radius. To deal with this limitation, many methods [4], [5] simultaneously estimate the wave velocity and pipe radii. However, the perpendicular

scanning constraint remains which is difficult to be satisfied in real-world applications. Recently, Li *et al.* [13] proposed an approach to estimate features of the buried pipelines without the requirement of perpendicular scanning. However, only an approximate model is proposed, and the approach has not considered multiple pipeline case.

A GPR generates hyperbola response when perpendicularly scanning over a cylindrical object. Pipeline mapping is actually the detection and analysis of hyperbolas. The commonly used hyperbola detection methods include conic fitting method [14], machine learning-based method [15], [16], and Hough transform-based method [17]. Most conic fitting methods can only identify one conic in each image and are often sensitive to outliers. Although the probabilistic hyperbola mixture model [18] is proposed to deal with these problems, the data partition in noisy GPR images before hyperbola fitting is still problematic. Results from machine learning methods depend on the quality of manually labeled training sets for different settings which are difficult to obtain in applications. Hough transform-based methods need to repeat with different parameter combinations to search the best hyperbola and are quite time consuming. Furthermore, it is difficult to specify a suitable threshold for the number of votes to determine the number of hyperbolas in the process. To deal with these problems, our method builds on a new GPR sensing model, the fusion of vSLAM, encoder, and GPR, and the integration of J-linkage and MLE. The approach does not require prior knowledge about the total number of hyperbolas or pipelines.

To map multiple pipelines, the 3D location of the detected pipelines needs to be georegistered to a spatial referencing system for further filtering. Combining GPR and GPS is posed in recent work [13]. However, GPS signals are often challenged in urban environments. Chen and Cohn [19] propose a pipeline mapping approach by fusing GPR detection results with existing utility records. However, the method inherently depends on both the quality and the availability of utility records. Our method employs a fixed on-board camera to localize itself and the GPR based on vSLAM technique [20], which requires minimal to zero prior knowledge and is less restricted by environments.

Our group has worked on both surface and subsurface infrastructure inspection using a robotic sensing suite for several years [21], [22]. The sensing suite contains a camera, a wheel encoder, and a GPR. Accurate calibration is the foundation of multiple sensor fusion for our subsurface inspection task. To fuse the three sensor modalities properly, we first design a calibration rig, model the GPR imaging system, introduce a mirror to obtain the joint coverage between the GPR and the camera, and employ the maximum likelihood estimator to estimate the relative pose between the GPR and the camera [23], [24]. Second, we propose a data collection scheme using the customized artificial landmarks to synchronize GPR/encoder data and camera images, and we also employ pose graph optimization with location discrepancy as penalty functions to perform data fusion [25]. The above-mentioned works lay a foundation for this article. This article improves our previous conference paper [26] by removing the assumption about planar ground surface, adding

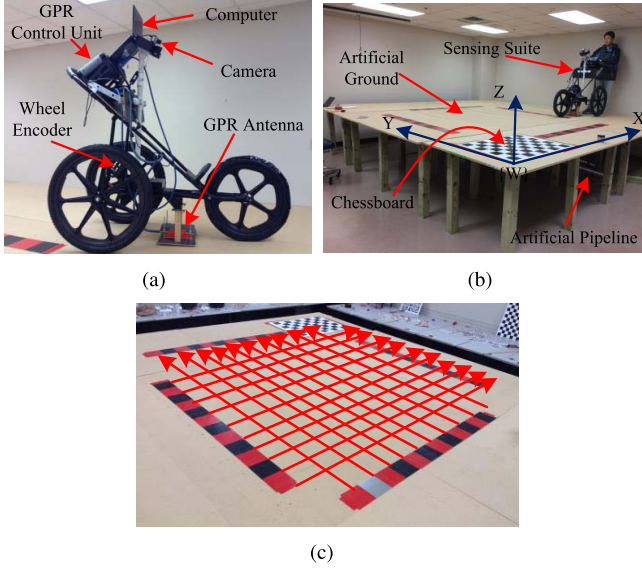


Fig. 2. (a) Our sensing suite on a tricycle, (b) experiment setup, and (c) grid-based scanning pattern contains two parallel groups that are perpendicular to each other.

pulse response extraction, performing error propagation analysis, analyzing the algorithm complexity, and conducting more field experiments. Compared with the conference version, the supplementary theoretical contributions mentioned earlier extend the application scope. Furthermore, in the experiment, the average localization error is slightly descended (4.47 cm versus 4.69 cm), and more importantly, more field tests have validated the robustness of our improved method more convincingly.

III. PROBLEM FORMULATION

Fig. 2(a) shows our sensing suite design which mounts a GPR and a camera on a tricycle. To focus on the horizontal pipeline mapping, we have the following assumptions.

Assumption 1: All pipelines can be approximated as piecewise connected cylinders whose centerlines intersect the horizontal plane with an angle less than 45° , since a GPR cannot distinguish pipes that are close-to-vertical and most pipeline segments are horizontal anyway.

Assumption 2: Pipelines are buried in a homogeneous medium, and the radio wave propagation velocity is priorly known from calibration.

During scanning, the GPR transmitting antenna emits polarized high-frequency pulses into the soil [see Fig. 3(a)]. When reaching an object with different electromagnetic properties compared with its surrounding medium, the pulses are reflected back to GPR. Then, the GPR estimates the traveling time between the emitted pulses and the echoed pulses and generates an A-scan [Fig. 3(b)] that records the signal amplitude versus traveling time at this GPR position. Based on Assumption 2, the traveling time can be converted into the traveling distance. While the GPR moves on the ground to perform scanning, it produces a series of A-scans at different positions. This ensemble of A-scans forms a B-scan [Fig. 3(c)]. A collection of B-scans combining with images

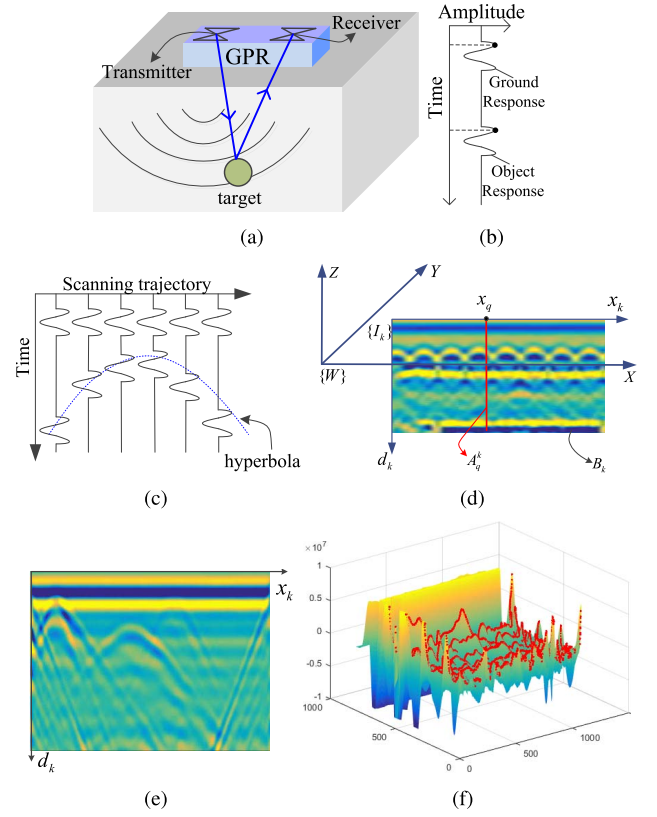


Fig. 3. Illustration of GPR working principle and coordinate system. (a)–(c) Ball-shaped object registers itself as a hyperbola in B-scan. (d) Coordinate systems and important notations. (e) Typical B-scan 2D view. (f) Sample B-scans 3D view with peaks marked by combining parallel scanning results.

captured by the camera at different scanning positions serve as inputs. To describe them, we define the following notations.

- 1) $\{W\}$, the 3D world coordinate system with X – Y plane representing the horizontal ground plane and z -axis pointing to the upward direction [see Fig. 3(d)]. A 3D point in $\{W\}$ is denoted as $\mathbf{X}^W \in \mathbb{R}^3$.
- 2) $A_q^k = \{a_t | t = 1, \dots, n_q\}$, the q th A-scan belonging to the k th B-scan, where t is the traveling time, a_t is the signal amplitude, and n_q is the number of readings.
- 3) $B_k = \{A_q^k | q = 1, \dots, n_k\}$, the k th B-scan consisting of n_k A-scans. Each B-scan can be viewed as a 2D image, where each $A_q^k \in B_k$ is a column of pixels. Note that this 2D GPR image is in an Euclidean coordinate because each pixel position $\mathbf{x} = [x_k, d_k]^T \in \mathbb{R}^2$ is in physical units of meters with x_k -axis parallel to the GPR moving direction, representing the distance traveled, and d_k -axis indicating the distance from GPR to object. Its origin is at the position of the first A-scan in B_k [see Fig. 3(d)].
- 4) $H_k = \{\mathbf{H}_j | j = 1, \dots, n_h\}$, the set of hyperbolas extracted from B_k , with each \mathbf{H}_j , $1 \leq j \leq n_h$ being the parameter vector of a hyperbola.
- 5) $\mathbf{L}_p = [r_p, (\mathbf{X}_{p,1}^W)^T, \dots, (\mathbf{X}_{p,n_p}^W)^T]^T$, the p th pipeline segment with its radius equal to r_p , $\mathbf{X}_{p,j}^W$, $j = 1, \dots, n_p$ representing the j th reconstructed point in $\{W\}$.
- 6) $\Omega = \cup\{\mathbf{L}_p\}$, the detected pipeline set.

Our pipeline mapping problem is defined as follows.

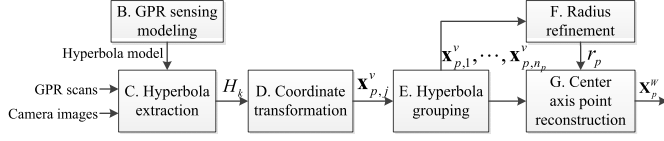


Fig. 4. System diagram. Each box index letter corresponds to Sections IV-B–IV-G.

Definition 1: Given synchronized camera images and GPR B-scans, extract hyperbola set H_k from each B_k , obtain Ω .

IV. ALGORITHM

Our system diagram is shown in Fig. 4. The system inputs are the synchronized GPR scans and camera images. We derive a sensing model which establishes hyperbola-shaped radar signals when the GPR scans a straight pipeline along a linear trajectory. The model allows us to extract hyperbolas from each B_k . Fused with vSLAM and encoder readings, the detected hyperbola vertices in all B_k 's are transformed into $\{W\}$. Then, our algorithm classifies hyperbolas into different groups according to their residing pipelines. Finally, for each pipeline group, we estimate pipe radius and locations. We begin with the data collection step.

A. Data Collection and GPR Data Rectification

Both the GPR and the camera are fixed on a sensing suite [see Fig. 2(c)] which moves along a straight line to collect data if the ground is planar. To guarantee the reconstruction accuracy, it is necessary to ensure that the intersection angle between the scanning trajectory and pipeline center lines projected to the horizontal plane is between 45° and 90° . Therefore, the scan follows a grid pattern in the horizontal plane which consists of evenly spaced survey lines in two parallel groups that are perpendicular to each other for pipeline mapping [see Fig. 2(c)]. It is obvious that we must have one group with the intersection angle no less than 45° even we do not know actual pipe orientation in the horizontal plane. This group can be easily identified in GPR readings. Hence, we assume all data are from this group in the rest of this article, which means all B_k 's are taken from parallel scans.

If the ground is nonplanar (see Fig. 5), we only need to ensure that the projections of GPR trajectories to the horizontal plane are from the two parallel groups. Although nonlinear in 3D [Fig. 5(a)], these trajectories are still straight lines if projecting to 2D horizontal space. According to GPR's working principle, it only records the traveling time of reflected waves (traveling time can be converted into distance if signal velocity is known). Therefore, the reflected curve generated by a pipeline in B-scan is no longer a hyperbola [Fig. 5(b)] when GPR travels on the nonplanar ground. Since GPR maintains the same distance to the ground during scanning, the ground reflection is still a straight band as indicated by the dark blue banded region on the top part of Fig. 5(b). To rectify this distortion, we can process each A-scan by realigning its Z-values in $\{W\}$ to an equal planar ground height, which is done by vertical offsetting A-scans using the ground height

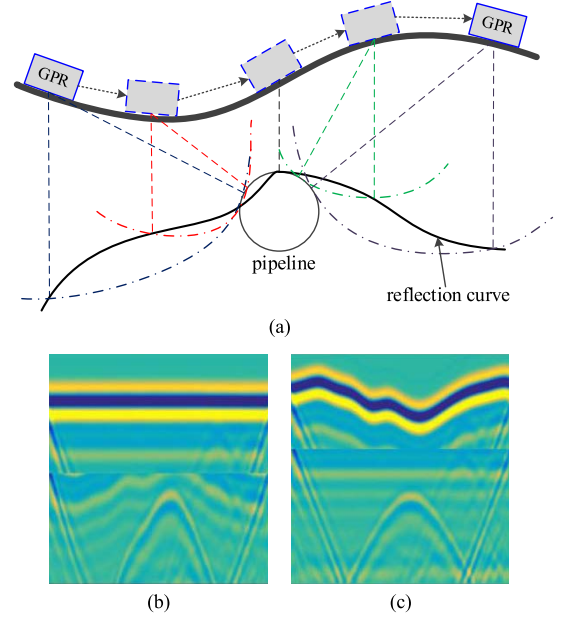


Fig. 5. Illustration of GPR data rectification for nonplanar ground distortion removal. (a) Declaration of GPR scan when moving on nonplanar ground. (b) Original B-scan. (c) Rectified B-scan.

from visual SLAM output. Fig. 5(c) shows the rectified B-scan for Fig. 5(b), where we can see the properly shaped hyperbola after the rectification.

In the rest of this article, all B-scans mentioned have their nonplanar ground distortion removed. Without loss of generality, we only need to focus on scans on a planar surface. Next, let us model the GPR sensing process in a single scan.

B. GPR Sensing Modeling

According to [4], horizontal cylindrical pipelines are recognized as hyperbolas in GPR scans. We explain it using a simple case when the GPR scans a pipeline perpendicularly before extending it to general cases with unknown orientations.

1) Perpendicular Scanning: Fig. 6(a) shows this ideal case. Let d_i be the distance measurement by the GPR at point x_i in B_k , x_v denotes the closest point to the pipeline on the scanning trajectory along x_k -axis, and d_v denotes the measured distance from x_v to the pipeline. The geometric relationship between the extracted hyperbola in B_k and the pipeline radius r is governed by the red right triangle formed at location x_v according to [28]

$$(d_i + r)^2 = (x_i - x_v)^2 + (d_v + r)^2. \quad (1)$$

We can rewrite (1) as the canonical hyperbola formulation

$$\frac{(d_i + r)^2}{(d_v + r)^2} - \frac{(x_i - x_v)^2}{(d_v + r)^2} = 1. \quad (2)$$

In fact, the point $[x_v, d_v]^T$ is the hyperbola vertex. However, in practice, the accurate orientation of pipelines is unknown. The probability of having a perpendicular scanning is negligible. A generic linear trajectory (GLT) usually does not have a known approaching angle to the pipeline centerline. We need a

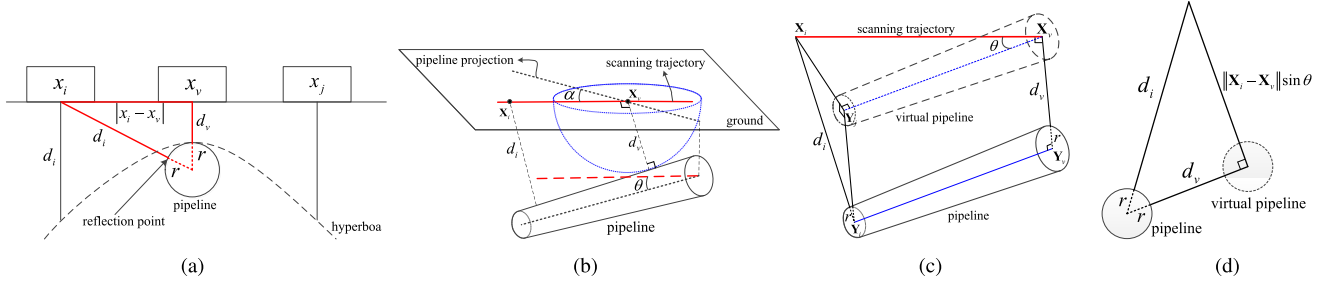


Fig. 6. Understanding GPR sensing model. (a) Perpendicular scanning. (b) GLT scanning. (c) Virtual pipeline. (d) 2D projection of (c).

sensing model for a GLT. More importantly, we need to know if the signal shape in the B-scan is still a hyperbola.

2) *GLT Sensing Model*: Fig. 6(b) shows that a GPR scans a pipeline along a GLT. Two angles, α and θ , are employed to describe the orientation of a straight pipeline segment, where α is the angle between the projection of the pipeline centerline on the X - Y plane of $\{W\}$ (i.e., ground plane) and the GLT, and θ is the angle between the pipeline and the GLT. Denote \mathbf{X}_i and \mathbf{X}_v as two 3D points on GLT in $\{W\}$ and \mathbf{X}_v is the closest point to the pipeline. The measured distances from \mathbf{X}_i and \mathbf{X}_v by the GPR are d_i and d_v , respectively. The following lemma presents the GPR sensing model when crossing the pipeline with a GLT.

Lemma 1: When the GPR scans the subsurface pipeline along a GLT, the resulting signal in a B-scan is the following hyperbola:

$$\frac{(d_i + r)^2}{(d_v + r)^2} - \frac{(x_i - x_v)^2 (\sin \theta)^2}{(d_v + r)^2} = 1 \quad (3)$$

where x_i and x_v denote the x -coordinate values in B_k when the GPR is located at \mathbf{X}_i and \mathbf{X}_v , respectively.

Proof: Fig. 6(b)–(d) shows the GLT scanning case. Denote $\overline{\mathbf{X}\mathbf{Y}}$ as the line segment connecting 3D points \mathbf{X} and \mathbf{Y} . We select two 3D points \mathbf{Y}_v and \mathbf{Y}_i lying on the center line of the pipeline, such that $\overline{\mathbf{X}_v\mathbf{Y}_v} \perp \overline{\mathbf{Y}_v\mathbf{Y}_i}$ and $\overline{\mathbf{X}_i\mathbf{Y}_i} \perp \overline{\mathbf{Y}_v\mathbf{Y}_i}$. Thus

$$\begin{aligned} \|\overline{\mathbf{X}_v\mathbf{Y}_v}\| &= d_v + r \\ \|\overline{\mathbf{X}_i\mathbf{Y}_i}\| &= d_i + r. \end{aligned}$$

We introduce a virtual pipeline $\overline{\mathbf{X}_v\mathbf{Y}_j}$ which is parallel to $\overline{\mathbf{Y}_v\mathbf{Y}_i}$ [see Fig. 6(c)]. Then, the angle between $\overline{\mathbf{X}_v\mathbf{X}_i}$ and $\overline{\mathbf{X}_v\mathbf{Y}_j}$ is θ , thus $\|\overline{\mathbf{X}_i\mathbf{Y}_j}\| = \|\overline{\mathbf{X}_v\mathbf{X}_i}\| \sin \theta$.

Since $\overline{\mathbf{X}_v\mathbf{Y}_v} \perp \overline{\mathbf{Y}_v\mathbf{Y}_i}$ and $\overline{\mathbf{Y}_v\mathbf{Y}_i} \parallel \overline{\mathbf{X}_v\mathbf{Y}_j}$, and thus, $\overline{\mathbf{X}_v\mathbf{Y}_v} \perp \overline{\mathbf{X}_v\mathbf{Y}_j}$. In addition, $\overline{\mathbf{X}_v\mathbf{Y}_v} \perp \overline{\mathbf{X}_v\mathbf{X}_i}$, and thus, $\overline{\mathbf{X}_v\mathbf{Y}_v}$ is perpendicular to the plane where \mathbf{X}_v , \mathbf{X}_i and \mathbf{Y}_j are lying on. Therefore, $\overline{\mathbf{X}_v\mathbf{Y}_v} \perp \overline{\mathbf{X}_i\mathbf{Y}_j}$. Since $\overline{\mathbf{X}_v\mathbf{Y}_v} \parallel \overline{\mathbf{Y}_i\mathbf{Y}_j}$, we can obtain that $\triangle \mathbf{X}_i\mathbf{Y}_i\mathbf{Y}_j$ is a right triangle. Projecting the scanning scenario into 2D view [see Fig. 6(d)], we have

$$(d_i + r)^2 = (\|\mathbf{X}_i - \mathbf{X}_v\| \sin \theta)^2 + (d_v + r)^2. \quad (4)$$

Since both $|x_i - x_v|$ and $\|\mathbf{X}_i - \mathbf{X}_v\|$ represent the same GPR traveling distance, we have $|x_i - x_v| = \|\mathbf{X}_i - \mathbf{X}_v\|$. Rewriting (4) in canonical hyperbola format, Lemma 1 is proven. \square

Lemma 1 shows that the resulting B-scan signals from scanning a pipeline along a GLT are still a hyperbola. Therefore, we can utilize this knowledge to extract them from noisy B-scans.

C. Hyperbola Extraction

The raw GPR data must be preprocessed before extracting hyperbolas. The preprocessing involves time-zero correction, average background subtraction, and low-pass filtering. According to [29] and [30], the distance between the first peaks of ground response and object response is the depth of the object [see the points in Fig. 3(b)]. Thus, to extract the hyperbola and the subsequent depth of the object, we need to find the peaks of the two types of response. To find the peaks accurately, we first extract the pulse responses generated by the ground and objects in each $A_q^k \in B_k$, by fitting a damped sinusoidal model [31], [32]. For the i th pulse response, we have

$$a_{t,i} = \beta_i e^{-\alpha_i t} \cos(\omega_i t + \phi_i) + \gamma_i \quad (5)$$

where $a_{t,i}$ is the signal amplitude at traveling time t , β_i is the amplitude, ω_i is the angular frequency, ϕ_i is the phase, γ_i is the offset for the model, and α_i is the attenuation constant defined by material properties.

With the pulse measurements $\{(t, a_{t,i}) | t \in \Gamma\}$, where Γ denotes the index set containing all measurements in the pulse, we can estimate the pulse responses from ground and objects in each $A_q^k \in B_k$ by solving the following optimization problem:

$$\begin{aligned} \arg \min_{\hat{\alpha}_i, \hat{\beta}_i, \hat{\gamma}_i, \hat{\omega}_i, \hat{\phi}_i} \sum_{t \in \Gamma} \|\hat{a}_{t,i} - a_{t,i}\|_{\Sigma}^2 \\ \text{s.t. } \hat{a}_{t,i} = \hat{\beta}_i e^{-\hat{\alpha}_i t} \cos(\hat{\omega}_i t + \hat{\phi}_i) + \hat{\gamma}_i \end{aligned} \quad (6)$$

where hat $\hat{\cdot}$ indicates the estimators and $\|\cdot\|_{\Sigma}$ denotes the Mahalanobis distance.

After obtaining these parameters, we can extract the peaks and the corresponding traveling times. Since the radio wave propagation velocity is priorly known according to Assumption 2, we can convert the traveling time into traveling distance. Define $\mathbf{x}_i = [x_i, d_i]^T$ be the i th peak position extracted from object responses in B_k , with x_i being the scanning distance in B_k and d_i being the signal traveling distance. Denote $M_k = \{\mathbf{x}_i | i = 1, \dots, n_m\}$ as the set of extracted peak points. Thus, our hyperbola detection problem is

Definition 2: Given M_k to Detect Multiple Hyperbolas.

Extracting hyperbolas from a GPR B-scan is nontrivial due to multiple solutions and significant noises as shown in Fig. 3(e) and (f). To find all hyperbolas, we apply the J-linkage [6] framework to detect them from each GPR B-scan. The J-linkage approach can simultaneously fit multiple models to data corrupted by noise and outliers without specifying the model number. Let us define $\mathbf{x}_{j,i} = [x_{j,i}, d_{j,i}]^T$ be the i th point lying on the j th hyperbola in B_k . Specially, we denote $[x_{j,v}, d_{j,v}]^T$ as the vertex of the hyperbola \mathbf{H}_j . We can represent the hyperbola form in Lemma 1 as

$$\tilde{\mathbf{x}}_{j,i}^T \mathbf{Q}_j \tilde{\mathbf{x}}_{j,i} = 0 \quad (7)$$

where $\tilde{\mathbf{x}}_{j,i} = [x_{j,i}, d_{j,i}, 1]^T$ is the homogeneous coordinate of $\mathbf{x}_{j,i}$, and

$$\mathbf{Q}_j = \begin{bmatrix} (\sin \theta)^2 & 0 & -x_{j,v}(\sin \theta)^2 \\ 0 & -1 & -r \\ -x_{j,v}(\sin \theta)^2 & -r & (\sin \theta)^2 x_{j,v}^2 + d_{j,v}^2 + 2d_{j,v}r \end{bmatrix}.$$

A generic conic, $ax^2 + bxy + cy^2 + dx + ey + f = 0$, has five DoFs. However, there are only four DoFs in our conic in (7) since the major axis of each hyperbola in B-scan is vertical which means $b = 0$. Thus, we can parameterize each hyperbola as

$$\mathbf{H}_j = [x_{j,v}, d_{j,v}, \sin \theta, r]^T. \quad (8)$$

Four points lying on the hyperbola are sufficient to compute a minimal solution of this hyperbola by solving (7).

In the J-linkage process, we first randomly choose M minimal sample set of four peak points to estimate the initial hyperbola by solving (7). For each initial hyperbola, if it satisfies $x_{j,v} > 0$ and $d_{j,v} > 0$, which indicates the vertex of the hyperbola located in the first quadrant of B_k , we consider it as a model hypothesis. Otherwise, we discard it.

For the rest, we follow the standard J-linkage steps which generate multiple clusters. For each cluster \mathcal{M}_j , if its size is greater than a threshold N_h , we accept this model hypothesis and further refine it from all peak points in \mathcal{M}_j . We model $\mathbf{x}_{j,i}$'s measurement error as a zero mean Gaussian with covariance matrix $\sigma_{j,i}^2 \mathbf{I}_2$, where \mathbf{I}_2 is a 2×2 identity matrix. Stacking all points in \mathcal{M}_j together, we obtain the following overall measurement error function

$$C_h(\mathbf{H}_j) = \begin{bmatrix} \tilde{\mathbf{x}}_{j,1}^T \mathbf{Q}_j \tilde{\mathbf{x}}_{j,1} \\ \vdots \\ \tilde{\mathbf{x}}_{j,m_j}^T \mathbf{Q}_j \tilde{\mathbf{x}}_{j,m_j} \end{bmatrix} \quad (9)$$

where $m_j = |\mathcal{M}_j|$ denotes the total point number in \mathcal{M}_j .

The MLE of \mathbf{H}_j can be obtained by minimizing the Mahalanobis distance

$$\mathbf{H}_j^* = \arg \min_{\mathbf{H}_j} C_h(\mathbf{H}_j)^T \sum_{H,j}^{-1} C_h(\mathbf{H}_j) \quad (10)$$

where $\sum_{H,j} = \text{diag}(\sigma_{j,1}^2, \dots, \sigma_{j,m_j}^2)$ is a diagonal matrix. This nonlinear optimization problem can be solved using Levenberg–Marquardt (LM) algorithm.

We also analyze the error of the estimated \mathbf{H}_j^* using the error backward propagation method [33] under Gaussian

assumptions. The estimation covariance matrix of \mathbf{H}_j^* , denoted as $\sum_{H_j^*}$, can be obtained as follows:

$$\sum_{H_j^*} = \left(J_h^T \sum_{H,j}^{-1} J_h \right)^{-1} \quad (11)$$

where $J_h = (\partial C_h / \partial \mathbf{H}_j)|_{\mathbf{H}_j = \mathbf{H}_j^*}$ is the Jacobian matrix.

Since \mathbf{H}_j contains $x_{j,v}$ and $d_{j,v}$, we can obtain the hyperbola vertex from \mathbf{H}_j^* . Let us define $\mathbf{v}_{p,j}^I = [x_{j,v}, d_{j,v}]^T$ to be the vertex of the j th hyperbola generated from the p th pipeline in the image coordinate system of B_k . Next, we need to classify and group the extracted hyperbolas in $\{W\}$ according to its pipe. This requires fusing with vSLAM and encoder readings.

D. Sensor Fusion for Coordinate Transformation

We project all hyperbola vertices onto the X - Y plane of $\{W\}$. Define $\mathbf{x}_{p,j}^v = [x_{p,j}^v, y_{p,j}^v]^T$ to be the corresponding position on X - Y plane in $\{W\}$ where the GPR receives $\mathbf{v}_{p,j}^I$. Here, we use the superscript v to indicate the vertex. We know $\mathbf{v}_{p,j}^I$ in B_k but finding $\mathbf{x}_{p,j}^v$ requires combining vSLAM outputs and wheel encoder data.

We denote the starting and ending points of the scanning line as $\mathbf{x}_{s,k} = [x_{s,k}, y_{s,k}]^T$ and $\mathbf{x}_{e,k} = [x_{e,k}, y_{e,k}]^T$, respectively, which are measured by the vSLAM algorithm. Note that they are 2D because all points are in X - Y plane with $z = 0$. We do not directly use $\mathbf{x}_{s,k}$ and $\mathbf{x}_{e,k}$ to localize $\mathbf{x}_{p,j}^v$ due to the vSLAM measurement errors. Since the GPR moves along a group of parallel GLTs according to Section IV-A, we adopt the parallelism constraint to refine $\mathbf{x}_{s,k}$ and $\mathbf{x}_{e,k}$. Denote $\hat{\mathbf{x}}_{s,k}$ and $\hat{\mathbf{x}}_{e,k}$ as the estimations of $\mathbf{x}_{s,k}$ and $\mathbf{x}_{e,k}$, respectively. Let us define

$$\mathbf{p}_v = [\mathbf{v}^T, (\hat{\mathbf{x}}_{s,1})^T, \dots, (\hat{\mathbf{x}}_{s,n})^T]^T$$

to be the parameter vector, where $\mathbf{v} = [v_x, v_y]^T$ is 2×1 directional vector with $\|\mathbf{v}\| = 1$, denoting the moving direction of all parallel trajectories, and n is total number of the parallel trajectories. Define l_k to be the length of the k th linear trajectory, which is obtained from wheel encoder readings. Thus

$$\hat{\mathbf{x}}_{e,k} = \hat{\mathbf{x}}_{s,k} + l_k \mathbf{v}. \quad (12)$$

We model both the covariance matrices of $\mathbf{x}_{s,k}$ and $\mathbf{x}_{e,k}$ as a zero mean Gaussian with covariance matrix $\sigma_v^2 \mathbf{I}_2$, where \mathbf{I}_2 is a 2×2 identity matrix. We estimate $\hat{\mathbf{x}}_{s,k}$, $k = 1, \dots, n$ and \mathbf{v} by minimizing the following cost function:

$$C_v(\mathbf{p}_v) = \begin{bmatrix} \hat{\mathbf{x}}_{s,1} - \mathbf{x}_{s,1} \\ \vdots \\ \hat{\mathbf{x}}_{s,n} - \mathbf{x}_{s,n} \\ \hat{\mathbf{x}}_{s,1} + l_1 \mathbf{v} - \mathbf{x}_{e,1} \\ \vdots \\ \hat{\mathbf{x}}_{s,n} + l_n \mathbf{v} - \mathbf{x}_{e,n} \end{bmatrix}. \quad (13)$$

We obtain the MLE of \mathbf{p}_v by solving the following optimization problem:

$$\mathbf{p}_v^* = \arg \min_{\mathbf{p}_v} C_v(\mathbf{p}_v)^T \sum_{C_v}^{-1} C_v(\mathbf{p}_v) \quad (14)$$

where $\Sigma_{C_v} = \text{diag}(\Sigma_{s,1}, \dots, \Sigma_{s,n}, \Sigma_{e,1}, \dots, \Sigma_{e,n})$ is a blockwise diagonal matrix and $\Sigma_{s,k}$ and $\Sigma_{e,k}$ denote the covariance matrices of $\mathbf{x}_{s,k}$ and $\mathbf{x}_{e,k}$, respectively. Here, we ignore the measurement errors from the wheel encoder because the wheel encoder is very accurate when the sensing suite moves on a flat ground. Again, this optimization problem can be solved by the LM algorithm.

With $\hat{\mathbf{x}}_{s,k}$ and $\hat{\mathbf{x}}_{e,k}$ obtained, we can obtain each hyperbola vertex position $\mathbf{x}_{p,j}^v$ in $\{W\}$ using the wheel encoder. We already know the wheel encoder increments between $\mathbf{x}_{p,j}^v$ and $\hat{\mathbf{x}}_{s,k}$ to be $x_{j,v}$. We also know the wheel encoder increments between $\hat{\mathbf{x}}_{s,k}$ and $\hat{\mathbf{x}}_{e,k}$ as $\|\hat{\mathbf{x}}_{e,k} - \hat{\mathbf{x}}_{s,k}\|$. Thus, the position of $\mathbf{x}_{p,j}^v$ is determined as

$$\mathbf{x}_{p,j}^v = \left(1 - \frac{x_{j,v}}{\|\hat{\mathbf{x}}_{e,k} - \hat{\mathbf{x}}_{s,k}\|}\right) \hat{\mathbf{x}}_{s,k} + \frac{x_{j,v}}{\|\hat{\mathbf{x}}_{e,k} - \hat{\mathbf{x}}_{s,k}\|} \hat{\mathbf{x}}_{e,k}. \quad (15)$$

Again, the covariance matrix of the estimated $\mathbf{x}_{p,j}^v$ can be obtained using error propagation methods in [33, Ch. 5].

We also analyze the error of the estimated $\mathbf{x}_{p,j}^v$. Since $\mathbf{x}_{p,j}^v$ is a function of $[(\hat{\mathbf{x}}_{s,k})^T, (\hat{\mathbf{x}}_{e,k})^T, x_{j,v}]^T$, its uncertainty depends on the noise distribution of $[(\hat{\mathbf{x}}_{s,k})^T, (\hat{\mathbf{x}}_{e,k})^T, x_{j,v}]^T$. Thus, we first compute the covariance matrices of $\hat{\mathbf{x}}_{s,k}$ and $\hat{\mathbf{x}}_{e,k}$, denoted as $\Sigma_{\hat{\mathbf{x}}_{s,k}}$ and $\Sigma_{\hat{\mathbf{x}}_{e,k}}$, respectively. We also denote the covariance of \mathbf{v} as Σ_v . According to the error backward propagation, we can obtain the covariance matrix of \mathbf{p}_v^* by

$$\Sigma_{\mathbf{p}_v^*} = \left(J_v^T \Sigma_{C_v}^{-1} J_v\right)^{-1} \quad (16)$$

where $\Sigma_{C_v}^{-1} = \text{diag}(\Sigma_{s,1}^{-1}, \dots, \Sigma_{s,n}^{-1}, \Sigma_{e,1}^{-1}, \dots, \Sigma_{e,n}^{-1})$ and $J_v = (\partial C_v(\mathbf{p}_v)/\partial \mathbf{p}_v)|_{\mathbf{p}_v=\mathbf{p}_v^*}$ is the Jacobian matrix, with

$$J_v = \frac{\partial C_v}{\partial \mathbf{p}_v} = \begin{bmatrix} \mathbf{0}_{2 \times 2} & \mathbf{I}_{2 \times 2} & \mathbf{0}_{2 \times 2} & \mathbf{0}_{2 \times 2} \\ \vdots & \mathbf{0}_{2 \times 2} & \ddots & \mathbf{0}_{2 \times 2} \\ \mathbf{0}_{2 \times 2} & \mathbf{0}_{2 \times 2} & \mathbf{0}_{2 \times 2} & \mathbf{I}_{2 \times 2} \\ l_1 \mathbf{I}_{2 \times 2} & \mathbf{I}_{2 \times 2} & \mathbf{0}_{2 \times 2} & \mathbf{0}_{2 \times 2} \\ \vdots & \mathbf{0}_{2 \times 2} & \ddots & \mathbf{0}_{2 \times 2} \\ l_n \mathbf{I}_{2 \times 2} & \mathbf{0}_{2 \times 2} & \mathbf{0}_{2 \times 2} & \mathbf{I}_{2 \times 2} \end{bmatrix}_{4n \times (2n+2)}.$$

Then, $\Sigma_{\hat{\mathbf{x}}_{s,k}}$, Σ_v , and the covariance matrix of $[(\hat{\mathbf{x}}_{s,k})^T, \mathbf{v}^T]^T$, denoted as $\Sigma_{\hat{\mathbf{x}}_{s,k}, \mathbf{v}}$, can be extracted from $\Sigma_{\mathbf{p}_v^*}$.

From (12), we know $\Sigma_{\hat{\mathbf{x}}_{e,k}}$ depends on the noise distribution of $\hat{\mathbf{x}}_{s,k}$ and \mathbf{v} . We obtain $\Sigma_{\hat{\mathbf{x}}_{e,k}}$ as

$$\Sigma_{\hat{\mathbf{x}}_{e,k}} = A_e \Sigma_{\hat{\mathbf{x}}_{s,k}, \mathbf{v}} A_e^T \quad (17)$$

where the matrix A_e is

$$A_e = \begin{bmatrix} 1 & 0 & l_k & 0 \\ 0 & 1 & 0 & l_k \end{bmatrix}.$$

According to (12), we can also derive the covariance of $[(\hat{\mathbf{x}}_{s,k})^T, (\hat{\mathbf{x}}_{e,k})^T]^T$ as

$$\Sigma_{\hat{\mathbf{x}}_{s,k}, \hat{\mathbf{x}}_{e,k}} = \begin{bmatrix} \Sigma_{\hat{\mathbf{x}}_{s,k}} & \Sigma_{s,e} \\ \Sigma_{s,e} & \Sigma_{\hat{\mathbf{x}}_{e,k}} \end{bmatrix} \quad (18)$$

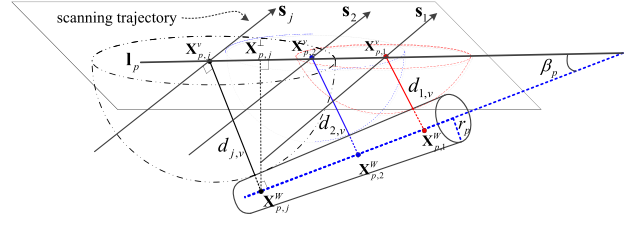


Fig. 7. An illustration of pipeline localization under parallel GLTs.

where

$$\Sigma_{s,e} = \frac{1}{2} \text{diag}(\sigma_{x_{e,k}}^2 + \sigma_{x_{s,k}}^2 - l_k \sigma_{v_x}^2, \sigma_{y_{e,k}}^2 + \sigma_{y_{s,k}}^2 - l_k \sigma_{v_y}^2)$$

with $\sigma_{x_{s,k}}^2, \sigma_{y_{s,k}}^2, \sigma_{x_{e,k}}^2$ and $\sigma_{y_{e,k}}^2$ being the variances of $\hat{x}_{s,k}, \hat{y}_{s,k}, \hat{x}_{e,k}$ and $\hat{y}_{e,k}$, respectively, $\sigma_{v_x}^2$ and $\sigma_{v_y}^2$ being the variances of \hat{v}_x and \hat{v}_y .

With $\Sigma_{\hat{\mathbf{x}}_{s,k}, \hat{\mathbf{x}}_{e,k}}$ obtained, we have

$$\text{cov}([(\hat{\mathbf{x}}_{s,k})^T, (\hat{\mathbf{x}}_{e,k})^T, x_{j,v}]^T) = \begin{bmatrix} \Sigma_{\hat{\mathbf{x}}_{s,k}, \hat{\mathbf{x}}_{e,k}} & \mathbf{0}^T \\ \mathbf{0} & \sigma_{x_{j,v}}^2 \end{bmatrix} \quad (19)$$

where $\text{cov}(\cdot)$ indicates the covariance matrix of a random vector, $\mathbf{0}$ denotes a 1×4 zero matrix, and $\sigma_{x_{j,v}}^2$ is the variance of $x_{j,v}$ which is already obtained in (11). Applying the first-order approximation of error forward propagation, we obtain the covariance matrix $\Sigma_{\mathbf{x}_{p,j}^v}$ of $\mathbf{x}_{p,j}^v$

$$\Sigma_{\mathbf{x}_{p,j}^v} = J_x \text{cov}([(\hat{\mathbf{x}}_{s,k})^T, (\hat{\mathbf{x}}_{e,k})^T, x_{j,v}]^T) J_x^T \quad (20)$$

where Jacobian matrix

$$J_x = \frac{\partial \mathbf{x}_{p,j}^v}{\partial (\hat{\mathbf{x}}_{s,k}, \hat{\mathbf{x}}_{e,k}, x_{j,v})} = \begin{bmatrix} 1 - \frac{x_{j,v}}{d_{es}} & 0 & \frac{x_{j,v}}{d_{es}} & 0 & \frac{x_{e,k} - x_{s,k}}{d_{es}} \\ 0 & 1 - \frac{x_{j,v}}{d_{es}} & 0 & \frac{x_{j,v}}{d_{es}} & \frac{y_{e,k} - y_{s,k}}{d_{es}} \end{bmatrix} \quad (21)$$

where $d_{es} = \|\hat{\mathbf{x}}_{e,k} - \hat{\mathbf{x}}_{s,k}\|$.

E. Hyperbola Grouping

Knowing hyperbola vertices in $\{W\}$ allow us to classify hyperbolas from multiple B_k 's into different groups according to their residing pipelines. This allows us to simultaneously detect multiple pipelines. Recall that we perform scanning by following parallel GLTs (see Fig. 7). Let $\mathbf{s}_j, j = 1, \dots, n_p$ represent the parallel GLTs crossing the p th pipeline, and thus, we have $\mathbf{s}_1 \parallel \mathbf{s}_2 \parallel \dots \parallel \mathbf{s}_{n_p}$. Recall that $\mathbf{x}_{p,j}^v = [x_{p,j}^v, y_{p,j}^v]^T$ is 2D point on X - Y plane of $\{W\}$ when the GPR receives the j th hyperbola vertex $[x_{j,v}, d_{j,v}]^T$ from the p th pipeline, and $\mathbf{x}_{p,j}^w$ is the j th center axis point on the p th pipeline, which is the closest axis point to \mathbf{s}_j . The following lemma presents the geometric model for center axis point reconstruction.

Lemma 2: If the GPR scans the p th pipeline along a set of parallel GLTs, \mathbf{s}_j , and $j = 1, \dots, n_p$, and produces the sequence of $\mathbf{x}_{p,j}^v, j = 1, \dots, n_p$ where the hyperbola vertices are perceived, as shown in Fig. 7, then all $\mathbf{x}_{p,j}^v, j = 1, \dots, n_p$ are collinear to a line on X - Y plane of $\{W\}$, denoted as \mathbf{l}_p ,

and the corresponding closest 3D center pipe axis points to each scanning GLT \mathbf{s}_j can be computed as follows:

$$\mathbf{X}_{p,j}^W = \begin{bmatrix} (1 - \lambda_{p,j})\mathbf{x}_{p,j}^v + \lambda_{p,j}\mathbf{x}_{p,j-1}^v \\ -(d_{j,v} + r_p) \cos \beta_p \end{bmatrix} \quad (22)$$

where r_p denotes the radius of the p th pipeline, β_p is the angle between \mathbf{l}_p and the pipeline centerline, and $\lambda_{p,j} = ((d_{j,v} + r_p) \sin \beta_p / \|\mathbf{x}_{p,j}^v - \mathbf{x}_{p,j-1}^v\|)$.

Proof: According to the working principle of GPR, for each \mathbf{s}_j , the hyperbola vertex is generated by the reflection of the pipeline surface point which is closest to \mathbf{s}_j . Thus, with $d_{j,v}$ known in each \mathbf{s}_j , all possible reflection points of the pipeline constitutes a hemisphere centered at $\mathbf{x}_{p,j}^v$ with radius equal to $d_{j,v}$, as shown in Fig. 7. The pipeline is tangential with all hemispheres.

Denote $\mathbf{X}_{p,j}^v = [(\mathbf{x}_{p,j}^v)^T, 0]^T$ as the 3D coordinate of $\mathbf{x}_{p,j}^v$, and $\overline{\mathbf{XY}}$ as the line segment connecting 3D points \mathbf{X} and \mathbf{Y} . For each \mathbf{s}_j , we have

$$\overline{\mathbf{X}_{p,j}^v \mathbf{X}_{p,j}^W} \perp \mathbf{s}_j$$

and

$$\begin{aligned} \overline{\mathbf{X}_{p,j}^v \mathbf{X}_{p,j}^W} &\perp \overline{\mathbf{X}_{p,1}^W \mathbf{X}_{p,n_p}^W} \\ \mathbf{s}_1 \parallel \mathbf{s}_2 \parallel \dots \parallel \mathbf{s}_{n_p} \\ \therefore \overline{\mathbf{X}_{p,1}^v \mathbf{X}_{p,1}^W} \parallel \dots \parallel \overline{\mathbf{X}_{p,n_p}^v \mathbf{X}_{p,n_p}^W}. \end{aligned}$$

\therefore all $\overline{\mathbf{X}_{p,j}^v \mathbf{X}_{p,j}^W}$, $j = 1, \dots, n_p$ are coplanar.

\therefore all $\mathbf{x}_{p,j}^v$, $j = 1, \dots, n_p$ are collinear.

With the line denoted as \mathbf{l}_p , it is clear that \mathbf{l}_p and $\overline{\mathbf{X}_{p,1}^W \mathbf{X}_{p,n_p}^W}$ are coplanar and intersect to each other. Furthermore, due to all \mathbf{s}_j , $j = 1, \dots, n_p$ are on the horizontal plane, the plane determined by $\mathbf{X}_{p,1}^W$, $\mathbf{X}_{p,j}^W$, and $\mathbf{X}_{p,j}^v$ is a vertical plane. Inside this vertical plane, there exists a vertical line passing $\mathbf{X}_{p,j}^W$ and intersecting \mathbf{l}_p at point $\mathbf{X}_{p,j}^\perp$ (see Fig. 7).

Connecting line segment $\overline{\mathbf{X}_{p,j}^W \mathbf{X}_{p,j}^\perp}$, we have

$$\overline{\mathbf{X}_{p,j}^W \mathbf{X}_{p,j}^\perp} \perp \overline{\mathbf{X}_{p,j}^v \mathbf{X}_{p,j-1}^v}.$$

Using trigonometry, we have

$$\begin{aligned} \|\mathbf{X}_{p,j}^v - \mathbf{X}_{p,j}^\perp\| &= (d_{j,v} + r_p) \sin \beta_p \\ \mathbf{X}_{p,j}^\perp &= \left(1 - \frac{(d_{j,v} + r_p) \sin \beta_p}{\|\mathbf{x}_{p,j}^v - \mathbf{x}_{p,j-1}^v\|}\right) \mathbf{x}_{p,j}^v \\ &\quad + \frac{(d_{j,v} + r_p) \sin \beta_p}{\|\mathbf{x}_{p,j}^v - \mathbf{x}_{p,j-1}^v\|} \mathbf{x}_{p,j-1}^v. \end{aligned}$$

Since $\mathbf{X}_{p,j}^\perp$ and $\mathbf{X}_{p,j}^W$ have the same X and Y coordinates, replacing the third element of $\mathbf{X}_{p,j}^\perp$ with $-(d_{j,v} + r_p) \cos \beta_p$, Lemma 2 is proven. \square

Lemma 2 implies that we can simultaneously detect multiple pipes by grouping the hyperbolas. It can be done by fitting multiple lines from the hyperbola vertex projection points. Again, the J-linkage framework is applied. Define $\tilde{\mathbf{x}}_{p,j}^v = [x_{p,j}^v, y_{p,j}^v, 1]^T$ to be the homogeneous form of $\mathbf{x}_{p,j}^v$. We denote \mathbf{l}_p as the 2D line projected from the p th pipeline

on X - Y plane of $\{W\}$. Any $\tilde{\mathbf{x}}_{p,j}^v$ generated from p th pipeline satisfies the following equation:

$$(\tilde{\mathbf{x}}_{p,j}^v)^T \mathbf{l}_p = 0. \quad (23)$$

A minimal solution requires two points. The rest follows the standard J-Linkage approach. After classifying the hyperbolas into different groups where all hyperbolas in the same group are generated from the same pipeline, we are ready to reconstruct pipelines with the grouped hyperbolas.

F. Pipeline Radius Refinement

Hyperbolas in the same group belong to the same pipeline and share the same radius. We can use this to refine the estimation of radius. Denote $r_{p,j}$, $j = 1, \dots, n_p$ as the estimated radius of the p th pipeline using the j th hyperbola by (10), with estimation variance σ_j^2 . Define r_p to be the radius of the p th pipeline. To estimate r_p optimally by combining all $r_{p,j}$'s, We define the following error function:

$$C_r(r_p) = \begin{bmatrix} r_p - r_{p,1} \\ \vdots \\ r_p - r_{p,n_p} \end{bmatrix}. \quad (24)$$

The MLE of r_p can be obtained by solving the following optimization problem:

$$r_p^* = \arg \min_{r_p} C_r(r_p)^T \sum_{r,p}^{-1} C_r(r_p) \quad (25)$$

where $\sum_{r,p} = \text{diag}(\sigma_1^2, \dots, \sigma_{n_p}^2)$ is a diagonal matrix.

G. Pipeline Center Axis Point Reconstruction

The final step is to estimate points $\mathbf{X}_{p,j}^W$ on the pipe center axis. Lemma 2 shows that we can obtain them from $\mathbf{X}_{p,j}^v$, \mathbf{l}_p and β_p . We use the geometric relationship to obtain them. Let us define the parameter vector to be estimated as

$$\mathbf{p} = [(\hat{\mathbf{x}}_{p,1}^v)^T, \dots, (\hat{\mathbf{x}}_{p,n_p}^v)^T, (\mathbf{l}_p)^T, \beta_p]^T$$

where $\hat{\mathbf{x}}_{p,j}^v$, $j = 1, \dots, n_p$ denotes the estimation of $\mathbf{x}_{p,j}^v$. Recall that $\mathbf{X}_{p,j}^v = [(\mathbf{x}_{p,j}^v)^T, 0]^T$. Then, we estimate \mathbf{p} by minimizing the following cost function:

$$C_p(\mathbf{p}) = \begin{bmatrix} \hat{\mathbf{x}}_{p,1}^v - \mathbf{x}_{p,1}^v \\ \vdots \\ \hat{\mathbf{x}}_{p,n_p}^v - \mathbf{x}_{p,n_p}^v \\ (\tilde{\mathbf{x}}_{p,1}^v)^T \mathbf{l}_p \\ \vdots \\ (\tilde{\mathbf{x}}_{p,n_p}^v)^T \mathbf{l}_p \\ \|\hat{\mathbf{x}}_{p,2}^v - \hat{\mathbf{x}}_{p,1}^v\| \sin \beta_p - (d_{2,v} - d_{1,v}) \\ \vdots \\ \|\hat{\mathbf{x}}_{p,n_p}^v - \hat{\mathbf{x}}_{p,1}^v\| \sin \beta_p - (d_{n_p,v} - d_{1,v}) \end{bmatrix}. \quad (26)$$

The MLE of \mathbf{p} can be obtained by solving the following problem:

$$\mathbf{p}^* = \arg \min_{\mathbf{p}} C_p(\mathbf{p})^T \sum_p^{-1} C_p(\mathbf{p}) \quad (27)$$

Algorithm 1: Pipeline Mapping and 3D Reconstruction

input : a set of camera images and $B_k, k = 1, \dots, n_k$
output: Ω

- 1 Extract Pulse responses from each A-scan; $O(n_b n_a)$
- 2 Detect Hyperbolas; $O(n_b n_p)$
- 3 Localize $\mathbf{x}_{s,k}$ and $\mathbf{x}_{e,k}$ for each scanning line; $O(f(n_l))$
- 4 Coordinate transform for each hyperbola vertex; $O(n_b)$
- 5 Group hyperbolas; $O(1)$
- 6 Estimate pipeline radius; $O(1)$
- 7 Reconstruct pipeline center axis points; $O(1)$
- 8 **return** Ω ; $O(1)$

where $\Sigma_p = \text{diag}(\Sigma_{p,1}^v, \dots, \Sigma_{p,n_p}^v, \lambda(\Sigma_{\tilde{x}_{p,1}}^v), \dots, \lambda(\Sigma_{\tilde{x}_{p,n_p}}^v), \sigma_{d,1}^2, \dots, \sigma_{d,n_p}^2)$ is a blockwise diagonal matrix. $\Sigma_{p,j}^v$ and $\Sigma_{\tilde{x}_{p,j}}^v$ are the covariance matrices of $\mathbf{X}_{p,j}^v$ and $\tilde{\mathbf{x}}_{p,j}^v$, respectively, which can be directly obtained according to $\Sigma_{p,j}^v$ as

$$\Sigma_{p,j}^v = \Sigma_{\tilde{x}_{p,j}}^v = \begin{bmatrix} \Sigma_{p,j}^v & 0 \\ 0 & 0 \end{bmatrix} \quad (28)$$

and $\lambda(\Sigma_{\tilde{x}_{p,j}}^v)$ denotes the maximum eigenvalue of $\Sigma_{p,j}^v \cdot \sigma_{d,j}^2$. $\sigma_{d,j}^2$ is the estimation variance of $(d_{j,v} - d_{1,v})$. Let us denote $\sigma_{d_{j,v}}^2$ as the estimation variance of $d_{j,v}$, which can be easily derived from (11). Then, we have $\sigma_{d,j}^2 = \sigma_{d_{j,v}}^2 + \sigma_{d_{1,v}}^2$.

With $\tilde{\mathbf{X}}_{p,j}^v$, \mathbf{I}_p , and β_p obtained, we can compute $\mathbf{X}_{p,j}^W$ based on Lemma 2.

V. ALGORITHM ANALYSIS

We summarize the proposed subsurface pipeline mapping and 3D reconstruction method in Algorithm 1 to facilitate our analysis. Let the total amount of B-scans be n_b . We suppose there are n_a A-scans in each B-scan on average. Then, extracting pulse responses can be done in $O(n_b n_a)$ time. Suppose on average we extract n_p pulse responses and n_h hyperbolas in each B-scan, then detecting hyperbolas can be done in $O(n_b n_p)$ time. Obviously, $n_p \geq n_a$ since we detect both ground pulse response and object pulse response in each A-scan. The value of n_h depends on the total number of pipelines. Thus, n_h is usually small and can be considered as constant. Localizing $\mathbf{x}_{s,k}$ and $\mathbf{x}_{e,k}$ involves the process of Oriented FAST and Rotated BRIEF (ORB)-SLAM, whose time complexity depends on landmarks in the environment. We define the total number of landmarks involved in ORB-SLAM is n_l . Then, the time complexity of ORB-SLAM process is $O(f(n_l))$, where $f(\cdot)$ denotes a function of n_l . Then, localizing the endpoints for all scanning lines can be done in $O(f(n_l))$ time. There are $n_b n_h$ hyperbola vertices in total. Since we consider n_h as constant, coordinate transform takes $O(n_b)$ time, and grouping hyperbolas takes $O(1)$ time. The time complexities of both estimating pipeline radii and reconstructing pipeline center axis points are $O(1)$. Thus, the computational complexity of our proposed pipeline mapping algorithm is $\max(O(n_b n_p), O(f(n_l)))$.

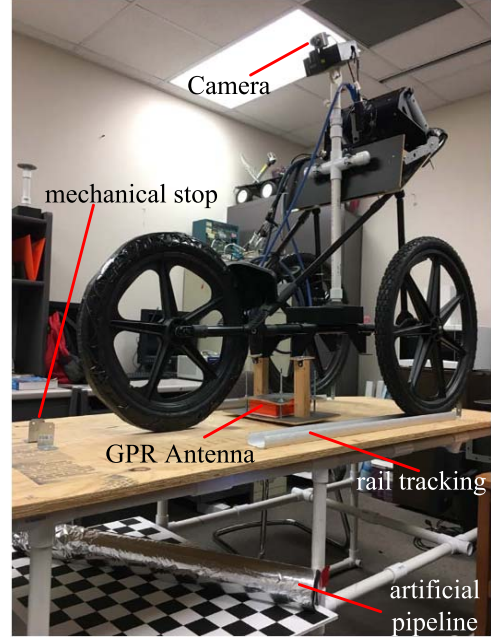


Fig. 8. Experiment setup for hyperbola model verification.

Theorem 1: The computational complexity of the proposed pipeline mapping and 3D reconstruction algorithm is $\max(O(n_b n_p), O(f(n_l)))$.

VI. EXPERIMENTS

We have implemented our algorithm using MATLAB under a PC. We use GSSI SIR-3000 GPR with 1.6 GHz antennas, and the parameters are given as follows: the horizontal sample rate for the wheel encoder is 390 pulses per meter, the two-way travel time of the radar signal is 8 ns, and the sample rate for the GPR is 1024 sample/scan. Each B-scan consists of 1643 A-scans on average. The camera used in the system is a 10-MP industry camera with model number DS-CFMT1000-H. The sensing suite is shown in Fig. 2(a).

We conduct two physical experiments—hyperbola model verification and field test for pipeline mapping. We begin with the verification of our proposed generic hyperbola model.

A. Hyperbola Model Verification

Since the generic hyperbola model proposed in Lemma 1 is the foundation of the following pipeline mapping, we verify it first. As shown in Fig. 8, we design an artificial planar bridge as the survey area under which an artificial pipeline with known parameters is placed. The bridge allows us to freely adjust the pipeline orientations underneath the bridge to generate different hyperbolas. We force the GPR to move along a fixed rail track with mechanical stops to guarantee each GPR scan repeating exactly the same trajectory. We can extract a hyperbola, denoted as $y = h(x)$, from each GPR scan. We also can derive a hyperbola equation, denoted as $y = \hat{h}(x)$, according to Lemma 1 by measuring the pipeline orientation. For comparison purpose, we define $y = \hat{g}(x)$ be the hyperbola derived using the model in (2) where GPR scans

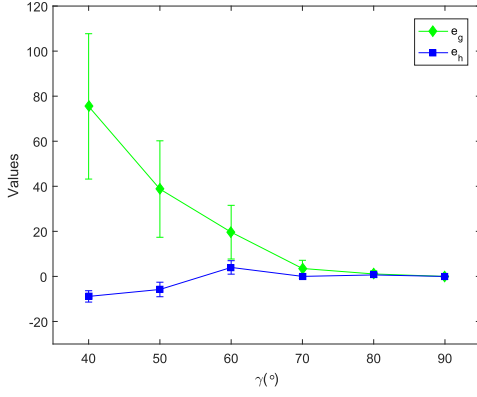


Fig. 9. Experiment results for hyperbola model verification. The marker position is the average value. The vertical bars correspond to $[-\sigma, \sigma]$ with σ as the standard deviation.

the pipeline perpendicularly. Define \underline{x} and \bar{x} are the start and end points of scanning, respectively. To evaluate the similarity between the extracted curve and the derived one, for each sample point $x \in [\underline{x}, \bar{x}]$, we define two error functions $e_h(x)$ and $e_g(x)$ to measure the difference between the extracted hyperbola with the derived model using Lemma 1 and the conventional model described in (2), respectively. More specifically

$$\begin{aligned} e_h(x) &= h(x) - \hat{h}(x) \\ e_g(x) &= h(x) - \hat{g}(x). \end{aligned} \quad (29)$$

We evenly select 50 sample points from \underline{x} to \bar{x} and compute $e_h(x)$ and $e_g(x)$ for each sample point $x \in [\underline{x}, \bar{x}]$. It is worth noting that the accurate GPR wave transmitting velocity is unknown when deriving the hyperbola equation according to Lemma 1 and the conventional model described in (2). Without loss of reasonableness, here, we adjust the velocity to find the best one which leads to the minimal average value of $e_h(x)$ and $e_g(x)$.

The statistical results for different pipeline orientations are shown in Fig. 9, where we can see that the average value of $e_h(x)$ at each orientation is very small and much smaller than the average value of $e_g(x)$. We did not give the results when $\gamma < 40^\circ$ because the accuracy of extracted hyperbola decreases greatly while the angle between pipeline with scanning direction becomes smaller. Furthermore, since we design our scanning trajectories as a grid with two orthogonal directions, at least the angle between pipeline with one scanning direction is no smaller than 45° . The average values of $e_h(x)$ are not zero due to the following factors: measurement errors in pipeline orientation and radius, and errors in hyperbola detection. However, the fact that the average value of $e_h(x)$ is close to 0 and smaller than $e_g(x)$ at each orientation validates that the model in Lemma 1 is correct.

B. Field Test for Pipeline Mapping

Since it is difficult to obtain the ground truth of the locations and sizes of the buried pipelines, we build a testbed platform so that we can place polyvinyl chloride (PVC) pipes underneath. The platform is a raised square artificial floor with a side

TABLE I
ALL PIPELINE ORIENTATION ESTIMATION ERRORS ($^\circ$)

No.	pipe 1		pipe 2		pipe 3		pipe 4	
	e_α	e_β	e_α	e_β	e_α	e_β	e_α	e_β
1	0.58	0.58	—	—	—	—	—	—
2	0.85	0.27	—	—	—	—	—	—
3	0.51	3.56	—	—	—	—	—	—
4	0.15	3.17	—	—	—	—	—	—
5	0.01	0.39	1.40	0.44	—	—	—	—
6	1.22	0.07	0.47	0.20	0.29	0.41	0.28	0.22
7	0.86	0.21	6.23	0.15	—	—	—	—
8	4.26	1.12	6.27	1.52	4.62	0.15	—	—
9	0.41	0.29	0.47	0.01	0.31	0.40	—	—
10	1.05	0.13	1.51	0.31	1.96	0.44	1.42	0.44
11	0.14	0.69	—	—	—	—	—	—
12	1.12	0.06	—	—	—	—	—	—
13	1.11	1.11	—	—	—	—	—	—
14	1.01	0.24	—	—	—	—	—	—
15	2.59	0.19	0.09	0	—	—	—	—
16	2.00	0.22	1.16	0.01	2.28	0.01	2.84	0.01
17	1.02	1.64	2.02	1.73	—	—	—	—
18	0.77	2.13	0.97	2.06	—	—	—	—
19	2.15	0.21	2.89	0.19	2.14	2.08	—	—
20	1.69	0.42	2.31	0.17	1.71	2.51	0.94	2.58
21	1.86	1.86	3.14	0.60	2.12	0.83	—	—
22	2.02	0.82	—	—	—	—	—	—
23	0.46	0.06	—	—	—	—	—	—
24	2.82	0.44	—	—	—	—	—	—
25	1.24	0.25	1.77	0.05	—	—	—	—
26	3.39	1.57	—	—	—	—	—	—
27	2.28	1.86	—	—	—	—	—	—
28	1.70	0.73	—	—	—	—	—	—
29	2.65	0.30	2.99	0.13	—	—	—	—
30	1.32	0.15	2.51	0.18	—	—	—	—

length of 5.5 m and a height of 0.9 m using wooden boards [see Fig. 2(b)]. To emulate the reflection signals from metal pipes, we wrap each PVC pipe with aluminum foil. Before GPR scanning, we first create a global map using ORB-SLAM [20] that covers the entire field, as shown in Fig. 2(c). The ground truth is manually measured using a tape measure with 1.59 mm accuracy.

In each setup, we change the PVC pipe number and configurations. We have finished all the 11 sets of different pipe configurations. The pipe configurations and the corresponding pictures are shown in Fig. 10. These 11 different configurations include most cases of real-utility pipeline configurations—one pipe with different orientations [Fig. 10(a)–(d)], multiple pipes with different radius [Fig. 10(e)–(k)], pipes in parallel [Fig. 10(e)–(h)] or intersect to each other [Fig. 10(i)–(k)], and create occlusion due to close proximity [Fig. 10(g)]. Two types of pipes are used in our experiments, with radii being 4.62 and 3.02 cm, respectively. In each setup, we move the sensing suite along parallel GLTs in the grid to collect the camera and GPR data following the synchronization method in [25]. Each GLT generates a B-scan and 98 camera images on average. In each setup, we have at least nine B-scans/GLTs. We have finished 30 experimental trials in all with these 11 different pipe configurations.

In our experiments, all pipelines are successfully detected. Fig. 11 presents a sample output for hyperbola extraction, where four hyperbolas are successfully detected from a noisy B-scan. As for mapping quality, we first examine the

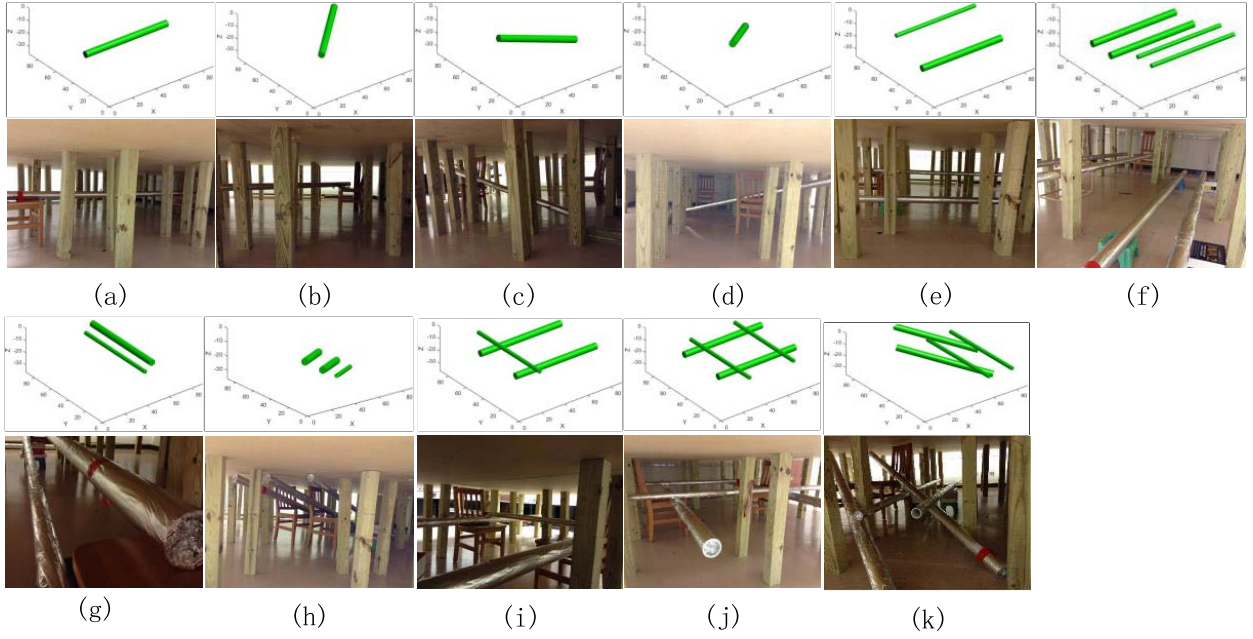


Fig. 10. Eleven representative pipe configurations in experiments.

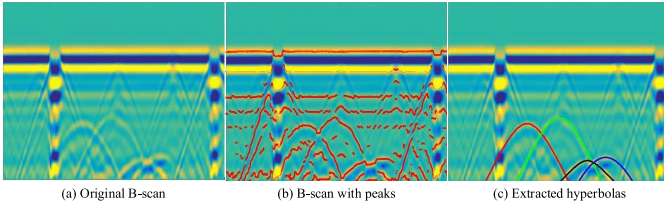


Fig. 11. Sample output for hyperbola extraction.

orientation of the detected pipelines. As shown in Fig. 7, we adopt two angles α_p and β_p to describe pipe orientations, where α_p is the angle between \mathbf{l}_p and the x -axis of $\{W\}$. We define e_α and e_β to be the estimation errors of α_p and β_p , respectively. The values of e_α and e_β for each pipe are presented in Table I. The average values of e_α and e_β are 1.73° and 0.73° , respectively. The maximum value of these two angle errors is 6.27° and 3.56° , respectively. These small errors mean that the pipeline orientation estimation accuracy is satisfying.

Next, we examine the quality of the reconstructed center axis point $\mathbf{X}_{p,j}^W$ where we compute the Euclidean distance from $\mathbf{X}_{p,j}^W$ to the ground-truth value of pipeline's centerline, denoted as error e_x . There are totally 58 pipes in our 30 experimental trials. We number them from 1 to 58 following the order of experiments. Fig. 12(a) presents the statistical results of e_x for each pipe, where the marker position is the average value, and the vertical bars correspond to $[-\sigma, \sigma]$ with σ as the standard deviation. The overall average localization error is 4.47 cm. Our pipeline localization algorithm is successful.

We define the metric $e_r = (|\hat{r} - \bar{r}|/\bar{r})$ to evaluate the pipeline radius estimation results, where \hat{r} and \bar{r} are the radius estimation result and the corresponding ground-truth value, respectively, and $|\cdot|$ denotes the absolute value operator.

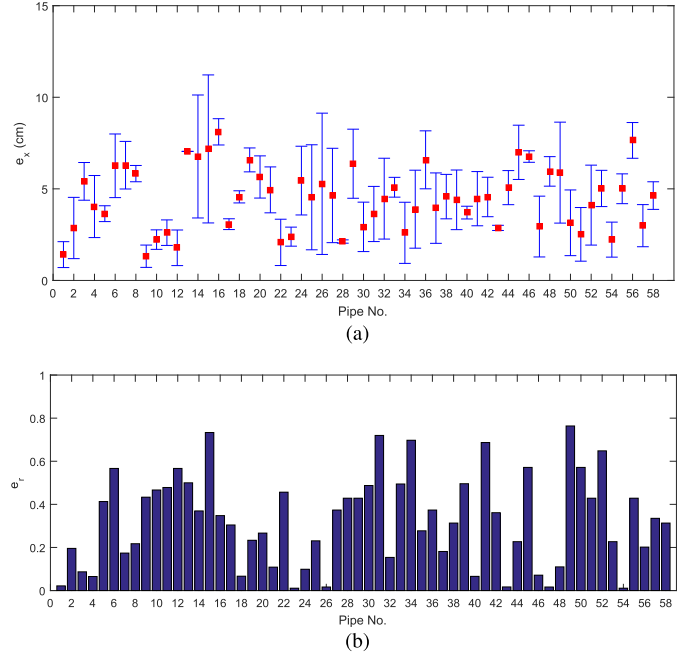
Fig. 12. Pipeline reconstruction results. (a) e_x statistical error. (b) Radius estimation relative error.

Fig. 12(b) presents the values of e_r for the 58 pipelines. The average value of e_r is 32.6%. This is expected because pipes used in our experiment are relatively thin in diameters. The localization error of 4.47 cm is quite significant in comparison to pipe diameters. The estimation errors are due to many factors, such as GPR accuracy limitation, hyperbola detection errors, the calibration error of GPR wave velocity, and the GPR scan localization errors. However, in most practical applications, the radii of pipelines are either prior known or conformal to typical standard sizes. As long as the result can

assist in finding the standard size, it is sufficiently accurate and acceptable.

VII. CONCLUSION AND FUTURE WORK

We reported a novel subsurface pipeline mapping method by fusing GPR scans and camera images. The camera images and encoder readings were used to provide the global position for each GPR scan so that our algorithm can simultaneously map multiple lines without assuming perpendicular scanning. We derived a GPR sensing model that proves hyperbola formulation under GLTs. Then, we developed a multiple hyperbola extraction algorithm under the J-linkage framework to detect and classify the hyperbolas generated from multiple pipelines. Finally, we optimally estimated the orientations, radii, and locations of all pipelines by analyzing the extracted hyperbolas. We tested our method in 30 groups of physical experiments with 11 different representative pipeline configurations. The results showed that our method successfully reconstructed all subsurface pipes.

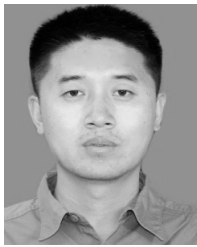
In the future, we will conduct more physical experiments in various scenarios. We also plan to relax the constraint further that requires the GPR to move linearly on flat ground by developing in-depth sensor fusion and GPR signal processing methods. The developments will significantly increase system deployment flexibility and applicability. We will develop efficient searching algorithms to reduce scanning time and trajectory length through better motion planning for searching pipelines.

ACKNOWLEDGMENT

The authors would like to thank H. Cheng, S. Yeh, A. Kingery, and A. Angert for their inputs and contributions to the Networked Robots Laboratory at Texas A&M University, College Station, TX, USA.

REFERENCES

- [1] P. Zhang, X. Guo, N. Muhammad, and X. Wang, "Research on probing and predicting the diameter of an underground pipeline by GPR during an operation period," *Tunnelling Underground Space Technol.*, vol. 58, pp. 99–108, Sep. 2016.
- [2] C. Windsor, L. Capineri, P. Falorni, S. Matucci, and G. Borgioli, "The estimation of buried pipe diameters using ground penetrating radar," *Insight-Non-Destructive Test. Condition Monitor.*, vol. 47, no. 7, pp. 394–399, 2005.
- [3] W. Al-Nuaimy, Y. Huang, M. Nakhkash, M. T. C. Fang, V. T. Nguyen, and A. Eriksen, "Automatic detection of buried utilities and solid objects with gpr using neural networks and pattern recognition," *J. Appl. Geophys.*, vol. 43, nos. 2–4, pp. 157–165, 2000.
- [4] C. Maas and J. Schmalz, "Using pattern recognition to automatically localize reflection hyperbolas in data from ground penetrating radar," *Comput. Geosci.*, vol. 58, pp. 116–125, Aug. 2013.
- [5] W. Li, H. Zhou, and X. Wan, "Generalized Hough transform and ANN for subsurface cylindrical object location and parameters inversion from GPR data," in *Proc. IEEE 14th Int. Conf. Ground Penetrating Radar (GPR)*, Jun. 2012, pp. 281–285.
- [6] R. Toldo and A. Fusiello, "Robust multiple structures estimation with j-linkage," in *Proc. Eur. Conf. Comput. Vis.* Berlin, Germany: Springer, 2008, pp. 537–547.
- [7] T. Hao *et al.*, "Condition assessment of the buried utility service infrastructure," *Tunnelling Underground Space Technol.*, vol. 28, pp. 331–344, Mar. 2012.
- [8] Y.-J. Liu, J.-B. Zhang, J.-C. Hou, J.-C. Ren, and W.-Q. Tang, "Cylinder detection in large-scale point cloud of pipeline plant," *IEEE Trans. Vis. Comput. Graphics*, vol. 19, no. 10, pp. 1700–1707, Oct. 2013.
- [9] A. C. D. Royal *et al.*, "Site assessment of multiple-sensor approaches for buried utility detection," *Int. J. Geophys.*, vol. 2011, Apr. 2011, Art. no. 496123.
- [10] H. Herman, "Robotic subsurface mapping using ground penetrating radar," Ph.D. dissertation, Robot. Inst., Carnegie Mellon Univ., Pittsburgh, PA, USA, 1997.
- [11] M. A. González-Huici, I. Catapano, and F. Soldovieri, "A comparative study of GPR reconstruction approaches for landmine detection," *IEEE J. Sel. Topics Appl. Earth Observ. Remote Sens.*, vol. 7, no. 12, pp. 4869–4878, Dec. 2014.
- [12] R. Janning, A. Busche, T. Horváth, and L. Schmidt-Thieme, "Buried pipe localization using an iterative geometric clustering on GPR data," *Artif. Intell. Rev.*, vol. 42, no. 3, pp. 403–425, 2014.
- [13] S. Li, H. Cai, D. M. Abraham, and P. Mao, "Estimating features of underground utilities: Hybrid GPR/GPS approach," *J. Comput. Civil Eng.*, vol. 30, no. 1, 2016, Art. no. 04014108.
- [14] A. Fitzgibbon, M. Pilu, and R. B. Fisher, "Direct least square fitting of ellipses," *IEEE Trans. Pattern Anal. Mach. Intell.*, vol. 21, no. 5, pp. 476–480, May 1999.
- [15] E. Pasolli, F. Melgani, and M. Donelli, "Automatic analysis of GPR images: A pattern-recognition approach," *IEEE Trans. Geosci. Remote Sens.*, vol. 47, no. 7, pp. 2206–2217, Jul. 2009.
- [16] Q. Dou, L. Wei, D. R. Magee, and A. Cohn, "Real-time hyperbola recognition and fitting in GPR data," *IEEE Trans. Geosci. Remote Sens.*, vol. 55, no. 1, pp. 51–62, Jan. 2017.
- [17] A. Simi, S. Bracciali, and G. Manacorda, "Hough transform based automatic pipe detection for array GPR: Algorithm development and on-site tests," in *Proc. IEEE Radar Conf. RADAR*, May 2008, pp. 1–6.
- [18] H. Chen and A. G. Cohn, "Probabilistic robust hyperbola mixture model for interpreting ground penetrating radar data," in *Proc. IEEE Int. Joint Conf. Neural Netw. (IJCNN)*, Jul. 2010, pp. 1–8.
- [19] H. Chen and A. G. Cohn, "Buried utility pipeline mapping based on multiple spatial data sources: A Bayesian data fusion approach," in *Proc. IEEE IJCAI*, vol. 11, Jul. 2011, pp. 2411–2417.
- [20] R. Mur-Artal, J. M. M. Montiel, and J. D. Tardós, "ORB-SLAM: A versatile and accurate monocular SLAM system," *IEEE Trans. Robot.*, vol. 31, no. 5, pp. 1147–1163, Oct. 2015.
- [21] Y. Lu, D. Song, H. Li, and J. Liu, "Automatic recognition of spurious surface in building exterior survey," in *Proc. IEEE Int. Conf. Autom. Sci. Eng.*, Madison, WI, USA, Aug. 2013, pp. 1047–1052.
- [22] H. Li, D. Song, Y. Liu, and B. Li, "Automatic pavement crack detection by multi-scale image fusion," *IEEE Trans. Intell. Transp. Syst.*, vol. 20, no. 6, pp. 2025–2036, Jun. 2019.
- [23] C. Chou, S.-H. Yeh, J. Yi, and D. Song, "Extrinsic calibration of a ground penetrating radar," in *Proc. IEEE Int. Conf. Autom. Sci. Eng. (CASE)*, Aug. 2016, pp. 1326–1331.
- [24] C. Chou, S.-H. Yeh, and D. Song, "Mirror-assisted calibration of a multi-modal sensing array with a ground penetrating radar and a camera," in *Proc. IEEE/RSJ Int. Conf. Intell. Robots (IROS)*, Vancouver, BC, Canada, Sep. 2017, pp. 1457–1463.
- [25] C. Chou, A. Kingery, D. Wang, H. Li, and D. Song, "Encoder-camera-ground penetrating radar tri-sensor mapping for surface and subsurface transportation infrastructure inspection," in *Proc. IEEE Int. Conf. Robot. Autom. (ICRA)*, Brisbane, QLD, Australia, May 2018, pp. 1452–1457.
- [26] H. Li, C. Chou, L. Fan, B. Li, D. Wang, and D. Song, "Robotic subsurface pipeline mapping with a ground-penetrating radar and a camera," in *Proc. IEEE/RSJ Int. Conf. Intell. Robots (IROS)*, Madrid, Spain, Oct. 2018, pp. 3145–3150.
- [27] F. Yang, X. Qiao, Y. Zhang, and X. Xu, "Prediction method of underground pipeline based on hyperbolic asymptote of GPR image," in *Proc. IEEE 15th Int. Conf. Ground Penetrating Radar (GPR)*, Jun./Jul. 2014, pp. 674–678.
- [28] S. Shihab and W. Al-Nuaimy, "Radius estimation for cylindrical objects detected by ground penetrating radar," *Subsurface Sens. Technol. Appl.*, vol. 6, no. 2, pp. 151–166, 2005.
- [29] D. J. Daniels, *Ground Penetrating Radar*, 2nd ed. Edison, NJ, USA: IET, 2004.
- [30] *Concrete Handbook (mn72-367 Rev H)*. Geophys. Surv. Syst., Nashua, NH, USA, 2017.
- [31] D. Goodman and S. Piro, *GPR Remote Sensing in Archaeology*. Berlin, Germany: Springer, 2013.
- [32] G. S. Baker, T. E. Jordan, and J. Pardy, "An introduction to ground penetrating radar (GPR)," *Special Papers-Geol. Soc. Amer.*, vol. 432, p. 1, Jan. 2007.
- [33] R. Hartley and A. Zisserman, *Multiple View Geometry in Computer Vision*, 2nd ed. Cambridge, U.K.: Cambridge Univ. Press, 2003.



Haifeng Li received the Ph.D. degree in control theory and control engineering from Nankai University, Tianjin, China, in 2012.

He is currently an Associate Professor with the Department of Computer Science and Technology, Civil Aviation University of China, Tianjin. He has authored or coauthored over 30 technical articles. His research interests include computer vision, image processing, robotic sensing, multisensor fusion, robot localization, and navigation.



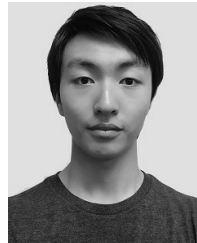
Binbin Li received the B.S. degree from the Department of Electrical Engineering and Automation, Harbin Institute of Technology, Harbin, China, in 2012. He is currently pursuing the Ph.D. degree in computer engineering with Texas A&M University, College Station, TX, USA.

His current research interests include the areas of robot vision and visual tracking and recognition.



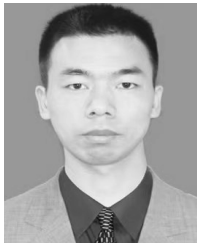
Chieh Chou (S'15) received the B.S. and M.S. degrees from the Department of Electronics Engineering, National Chiao Tung University, Hsinchu, Taiwan, in 2008 and 2010, respectively, and the Ph.D. degree from the Department of Computer Science and Engineering, Texas A&M University, College Station, TX, USA, in 2019.

His research interests include robot perception, robot vision, sensor fusion, and localization.



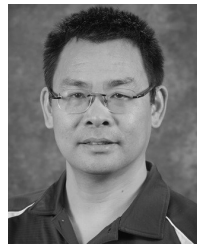
Di Wang received the B.E. degree in computer science from the Harbin Institute of Technology, Harbin, China, in 2017. He is currently pursuing the master's degree with Texas A&M University, College Station, TX, USA.

His research interests include computer vision, robotics, and sensor fusion.



Longfei Fan received the B.S. degree from the Department of Computer Science and Technology, Hebei Institute of Technology, Tianjin, China, in 2015.

He is currently an Experimentalist with the Department of Computer Science and Technology, Civil Aviation University of China, Tianjin. His current research interests include the areas of robot vision and image processing.



Dezhen Song (S'02–M'04–SM'09) received the Ph.D. degree in industrial engineering from the University of California at Berkeley, Berkeley, CA, USA, in 2004.

He is currently a Professor with the Department of Computer Science and Engineering, Texas A&M University, College Station, TX, USA. His research interests include networked robotics, distributed sensing, computer vision, surveillance, and stochastic modeling.

Dr. Song was a recipient of the Kayamori Best Paper Award of the 2005 IEEE International Conference on Robotics and Automation (with J. Yi and S. Ding). He was also a recipient of the NSF Faculty Early Career Development (CAREER) Award in 2007. From 2008 to 2012, he was an Associate Editor of the IEEE TRANSACTIONS ON ROBOTICS. From 2010 to 2014, he was an Associate Editor of the IEEE TRANSACTIONS ON AUTOMATION SCIENCE AND ENGINEERING. He is currently a Senior Editor of the IEEE ROBOTICS AND AUTOMATION LETTERS.